

Vertical profile of tropospheric ozone derived from synergetic retrieval using three different wavelength ranges, UV, IR, and Microwave: sensitivity study for satellite observation

Yasuko Kasai^{1,2}, Tomohiro O. Sato¹, Takao M. Sato^{3,1}, Hideo Sagawa⁴, Katsuyuki Noguchi⁵, Naoko Saitoh⁶, Hitoshi Irie⁶, Kazuyuki Kita⁷, Mona E. Mahani^{1,8}, Koji Zettsu¹, Ryoichi Imasu⁹, and Sachiko Hayashida⁵

¹National Institute of Information and Communications Technology, Tokyo, Japan

²Tokyo Institute of Technology, Tokyo, Japan

³Institute of Space and Astronautical Science, Japan Aerospace Exploration Agency, Kanagawa, Japan

⁴Kyoto Sangyo University, Kyoto, Japan

⁵Nara Women's University, Nara, Japan

⁶Center for Environmental Remote Sensing, Chiba University, Chiba, Japan

⁷Ibaraki University, Ibaraki, Japan

⁸Tohoku University, Sendai, Japan

⁹Atmospheric and Ocean Research Institute, The University of Tokyo, Chiba, Japan

Correspondence to: Y. Kasai (ykasai@nict.go.jp)

Abstract. We performed a quantitative feasibility study of constraining the vertical profile of the amount of ozone in the troposphere by using a synergetic retrieval method on multiple spectra, i.e., ultraviolet (UV), thermal infrared (TIR) and microwave (MW) ranges, measured from space. Twenty atmospheric scenarios for East Asia in summer and winter seasons were assumed in this study. Geometry of line-of-sight was nadir down-looking for UV and TIR measurements, and limb-sounding for MW measurement. The sensitivities of retrieved ozone in the upper troposphere (UT), middle troposphere (MT) and lowermost troposphere (LMT) were estimated using values of the degree of freedom for signal (DFS), partial column error, and averaging kernel matrix, derived based on the optimal estimation method. The measurement noises were assumed at the same level as the currently available instruments. The weighting functions for the UV, TIR and MW ranges were calculated using the SCIATRAN radiative transfer model, the Line-By-Line Radiative Transfer Model, and the Advanced Model for Atmospheric Terahertz Radiation Analysis and Simulation, respectively. In the UT region, the DFS value was enhanced by about 200 % by adding the MW measurements to the combination of UV and TIR measurements. We found that the DFS value of the LMT ozone was increased by approximately 40 % by adding the MW measurements to the combination of UV and TIR measurements; nevertheless, the MW measurement alone has no sensitivity for the LMT ozone. Better information of the LMT ozone can be educed by adding constraints on the UT and MT ozone from the MW measurement. The results of this study will be implemented in the Japanese air-quality monitoring missions, APOLLO, GMAP-Asia and uvSCOPE.

1 Introduction

The World Health Organization (WHO) estimates that around seven million people died as a result of the effects of air pollution in 2012 (WHO, 2014), and it cites air pollution as being one of the world's largest single environmental health risk. Ozone in particular causes serious damage for human health and agricultural crops. Tropospheric ozone has been increasing globally at rates of 0.3–1.0 ppb yr⁻¹ over past few decades in the northern hemisphere (Dentener et al., 2010, and references therein). Ozone is formed by sunlight-driven oxidation from ozone precursors such as methane (CH₄), carbon monoxide (CO), non-methane volatile organic compounds (NMVOCs), and nitrogen oxides (NO_x) in the troposphere. Monitoring of the amount of the tropospheric ozone is required to understand the current status and to make forecasts of future ozone amount.

Ozone plays different roles in different altitude regions in the troposphere. It is well known that surface ozone is a harmful pollutant that has a detrimental impact on the health of humans and plants and is responsible for significant reduction in crop yields. The lifetime of ozone in the free troposphere ranges from a few days to weeks, so that the transport scale of ozone is potentially intercontinental and hemispheric. Upper tropospheric ozone is the third most important warming gas and is responsible for a large part of the human enhancement of the global greenhouse effect. For further understanding these different characteristics of tropospheric ozone, it is important to obtain information on the vertical distribution of ozone separately in the lowermost troposphere (LMT), middle troposphere (MT), and upper troposphere (UT) on a global scale.

Ozone has been observed from space in a variety of spectral ranges, including the ultraviolet (UV), visible (VIS), thermal infrared (TIR), and microwave (MW) with different observation geometries (nadir-looking and limb-sounding). Observations at different wavelengths have sensitivity to ozone at different altitudes. Generally, nadir-looking observations in the UV/VIS range are sensitive to ozone in the LMT (e.g., the Ozone Monitoring Instrument, OMI, onboard the Aura satellite (Levelt et al., 2006) and the second Global Ozone Monitoring Experiment, GOME-2, onboard the MetOp satellite (Munro et al., 2006)), while nadir-looking in the TIR range is sensitive to ozone in the MT (e.g., the Thermal Emission Spectrometer, TES, onboard the Aura satellite (Osterman et al., 2008) and the Infrared Atmospheric Sounding Interferometer, IASI, onboard the MetOp satellites (Clerbaux et al., 2009)). Limb-sounding and stellar/solar-occultation is used to sound ozone in the stratosphere and above. Limb-sounding in the UV/VIS region sounds ozone in the stratosphere, and stellar occultation instruments observe ozone above the stratosphere (e.g., the Scanning Imaging Absorption Spectrometer for Atmospheric Chartography, SCIAMACHY, (Brinksma et al., 2006) and the Global Ozone Monitoring by Occultation of Stars, GOMOS, (Kyrölä et al., 2004) both onboard the Envisat satellite). Limb-sounding in the MW spectral range is sensitive at altitudes above the UT (e.g., the Microwave Limb Sounder, MLS, onboard the Aura satellite (Waters et al., 2006) and the Superconducting Submillimeter-Wave Limb-Emission Sounder, SMILES, onboard the International Space Station (Kikuchi et al., 2010)).

Measurement using several wavelength ranges is an advanced method of deriving a vertically resolved ozone profile. Ziemke et al. (2006) derived the global distribution of the tropospheric ozone column by subtracting the stratospheric ozone column measured using the MLS MW spectra from the total ozone column measured using the OMI UV spectra. A feasibility study of the tropospheric ozone retrieval using the optimal estimation method (OEM) (Rodgers, 2000) combining UV and TIR measurements was performed by Landgraf and Hasekamp (2007). Worden et al. (2007) implemented the concept of synergetic

retrieval on the OMI and TES measurements. Natraj et al. (2011) showed that the retrieval sensitivity of the LMT is improved by combining UV and TIR measurements. Fu et al. (2013) implemented a synergetic retrieval of boundary layer ozone using the UV and TIR spectra of the OMI and TES measurements. A value of the degree of freedom for signal (DFS) for ozone from the surface to 700 hPa was estimated to be 0.37 ± 0.09 for 22 coincident measurements among OMI, TES, and ozonesonde
5 from 2004 to 2008 (see Table 2 in Fu et al. (2013)). Cuesta et al. (2013) also performed a synergetic retrieval of boundary layer ozone, using the GOME-2 (for UV) and IASI (for TIR) measurements. Although the DFS value of boundary layer ozone is much improved by combining UV and TIR measurements, it is less than unity. **The other approach to retrieve the tropospheric ozone profile using neural network technique was performed with the SCIAMACHY nadir measurements in the UV and VIS ranges (Sellitto et al., 2012a, b). They also showed a significant availability of combining several wavelength ranges to retrieve**
10 **the tropospheric ozone profile.**

Our idea is to add MW measurements to the synergetic retrieval of the tropospheric ozone. To the best of our knowledge, no study has attempted to show how MW measurements improve the retrieval of the vertical profile of tropospheric ozone. In this study, we performed a feasibility study of obtaining a vertically resolved ozone amount in the troposphere by using synergetic retrieval from a combination of UV, TIR and MW measurements covering wide wavelength ranges. This work
15 can be of benefit to future missions for air-pollution, such as Air POLLution Observation (APOLLO), Geostationary mission for Meteorology and Air Pollution (GMAP-Asia) (Kasai et al., 2011), uvSCOPE (Fujinawa et al., 2015), and air pollution prediction project in National Institute of Information and Communication Technology (NICT). The objective of APOLLO and GMAP-Asia mission is to measure short-lived climate pollutants for monitoring global pollution and climate change. The missions of APOLLO and GMAP-Asia assume atmospheric monitoring from the International Space Station (ISS) and from
20 geostationary orbit, respectively. The uvSCOPE mission, a candidate for the earth observation section of ISS, aims to detect hot-spots of air pollutant with a high horizontal resolution (such as $1 \times 1 \text{ km}^2$) for better understanding of the inventory of air pollution. The target of NICT air pollution prediction project is to make health index to mitigation of air pollution disasters using high-horizontal resolution (a few km scale) pollution forecasting from multiple data-sets, such as satellite observation, ground-based observation, and in-situ observation data.

25 In this paper, we report a feasibility study of the tropospheric ozone retrieval based on the concept of APOLLO, i.e., to obtain vertically resolved information of ozone within the troposphere not only at the boundary layer but also in the middle and upper troposphere by utilizing synergetic observation afforded by UV, TIR and MW instruments.

2 Observation scenario

2.1 Observation wavelength region and geometry

30 The observation scenario follows the concept of the APOLLO mission. We assumed three spectrometers equipped in ISS that observe the three wavelength ranges of UV, TIR, and MW. Figure 1 shows the observation geometries for the three spectrometers. The UV and TIR instruments use nadir down-looking, and the MW measurement uses limb-sounding at tangent heights from 10 to 80 km. In this feasibility study, we assumed spherically homogeneous atmosphere along the line-of-sight

of the MW measurement. The height of ISS was assumed to be 300 km in our simulation. The target area of this study is East Asia, one of most serious ozone polluted areas on Earth and the source of ozone intercontinental transport toward North America from Asia. We chose two observation points in East Asia, 35°N, 116.5°E (Central-East China, CEC, located between Beijing and Shanghai) and 31°N, 127.25°E (East China Sea, ECS). The observation time was set to 04:00am GMT, which corresponds to 11:46am and 00:29pm for CEC and ECS local times, respectively. The azimuthal direction of the field-of-view of the MW limb-sounding was set to parallel to the ISS's orbital motion. The tangent point of the MW limb-sounding passes the UV and TIR nadir down-looking point approximately five minutes before the UV and TIR nadir down-looking. We ignored this time difference between the UV and TIR measurements and MW measurement. Table 1 is a summary of the specification of the three assumed instruments and the radiative transfer models used in this study.

The wavelength range of the simulation of the UV measurement was set to 305–340 nm. We decided not to include the VIS (340–505 nm) and the shorter UV spectral range (<305 nm) in this study, although the benefit of adding VIS wavelengths has been reported (e.g., Sellitto et al., 2012a, b). The reason why we excluded these ranges is because the wavelength dependence of the surface reflectance, absorption of NO₂ and the Ring effect were out of the scope of the study. The spectral resolution, defined as the full width at half maximum (FWHM), and the sampling step were assumed to be 0.6 nm and 0.2 nm, respectively. The noise equivalent spectral radiance (NESR) for a surface albedo of 90 % and the solar zenith angle of 0° were approximately 90 and 2600 at 300 and 340 nm, respectively (private communication with K. Gerilowski). The NESR value was obtained by dividing the simulated backscattered radiance by the signal-to-noise ratio (SNR).

We assumed that the nadir-viewing TIR instrument would be a Fourier transform spectrometer covering the TIR spectral range (980–1080 cm⁻¹) including the ozone ν₃ absorption band, 9.6 μm (1045 cm⁻¹) as TES (Osterman et al., 2008) and IASI (Boynard et al., 2009). We set the maximum optical path difference to 8.33 cm, which corresponds to a spectral resolution of 0.12 cm⁻¹ and calculated the noise equivalent differential temperature for each wavelength, assuming that the SNR is a constant value of 300 in the entire spectral range.

Several ozone transitions in the microwave/submillimeter range have been employed by recent space-borne instruments, e.g., 243.4 GHz for Aura/MLS (Waters et al., 2006), 501.8 and 544.6 GHz for Odin/SMR (Urban et al., 2005), and 625.3 GHz for JEM/SMILES (Kikuchi et al., 2010). The MW limb-sounding instrument considered in this study was designed for covering two frequency bands, i.e., the 350 GHz band (345–357 GHz) and 645 GHz band (639–651 GHz). There are ozone lines at 352.3, 352.8, and 355.0 GHz in the former and at 640.1, 642.3, 644.8, 645.6, 647.8, and 650.7 GHz in the latter. These frequency bands were selected for detection of not only ozone but also other molecules related to global warming and air-pollution (H₂O, CO, CH₃CN, N₂O, SO₂, H₂CO, and HNO₃). The channel separation width of the spectrometer was assumed to be 25 MHz. The frequency resolution, defined by FWHM was set to be identical to the channel separation width. The Earth's limb was assumed to be scanned vertically from 10 to 80 km with an interval of 2 km using a 40 cm diameter antenna. The brightness temperature noise was estimated to be 0.7 K and 1.7 K for the 350 GHz and 645 GHz bands, respectively, assuming the system noise temperature of a typical Schottky-barrier mixer (2500 K and 6000 K for 350 GHz band and 645 GHz band, respectively) and a typical integration time of 0.5 s for one spectrum accumulation.

2.2 Atmospheric conditions

We performed a feasibility study of tropospheric ozone retrieval for typical atmospheric scenarios in summer and winter. We made a total of 20 atmospheric scenarios from the model calculation and air-borne observations made over two Asian areas (CEC and ECS) in June and December 2009. The characteristics of the 20 atmospheric scenarios are presented in Table 2, and vertical profiles of ozone, temperature and water vapor are shown in Figure 2. We assumed the following quasi-clear sky cases for all scenarios. A no-cloud condition was considered for all wavelength ranges. Basic background aerosol was taken into account only in the UV calculation. We used the vertical profiles of urban and maritime aerosols of a standard mixing state that were described in Hess et al. (1998). The scale height of the vertical profiles that we used was 3 km. These profiles were adjusted to be 0.2 of the total optical thicknesses of the aerosols (moderate pollution).

We interpolated the values from the following three original atmospheric profiles by using cubic splines to make the atmospheric profile smooth in the overlapping regions for a vertical pressure (p) grid defined as follows.

$$p[i] = \begin{cases} 10^{3-(i+1)/24} \text{ [hPa]} & i = 1, 2, \dots, 71 (\geq 1 \text{ hPa}) \\ 10^{3-(i-35)/12} \text{ [hPa]} & i = 72, 73, \dots, 108 (< 1 \text{ hPa}) \end{cases}$$

The profiles of ozone, temperature, and water vapor in the vertical region from the surface to 65 hPa (approximately 20 km) were simulated by a one-way nested global-regional air quality forecasting (AQF) system (Takigawa et al., 2007, 2009). This system is based on the CHASER (Chemical Atmospheric General Circulation model for the Study of Atmospheric Environment and Radiative Forcing) model (Sudo et al., 2002) and WRF (Weather Research and Forecasting)/Chem model (Grell et al., 2005) version 3.3. The horizontal resolution of this system is approximately 40 km. The profiles over CEC and ECS were spatially averaged for the periods of June 1 to June 30 and December 1 to December 31, 2009. Twenty atmospheric profiles at 12:00 LT in the two areas were used in this study. The surface temperature was simulated with the AQF system, and the temperature difference between the surface and the lower boundary of the lowest atmospheric layer was less than 1 K. We set the surface temperature to be equal to the value at the surface pressure, since the effect of the temperature contrast between the atmosphere and surface is large for the TIR measurement.

The profiles (ozone, temperature and water vapor) in a vertical region of 985–0.01 hPa were taken from the Modern Era Retrospective-Analysis for Research and Applications (MERRA) data (Rienecker et al., 2011). A data product named “MERRA DAS 3d analyzed state (inst6_3d_ana_Nv)” provided the three-dimensional fields of layer pressure thickness, air temperature, specific humidity, and ozone mixing ratio at six-hour intervals (00:00, 06:00, 12:00, 18:00 GMT). The MERRA data covered a $0.66^\circ \times 0.5^\circ$ latitude-longitude grid. We averaged the MERRA data at 06:00 GMT (the nearest local time of 12:00 LT in CEC and ECS) on the same date of the selected AQF system profiles for each region (CEC and ECS). No interpolation for local time was performed on the MERRA data.

The temperature data of the COSPAR International Reference Atmosphere (CIRA) (Fleming et al., 1990) was used above the vertical level of 0.01 hPa. The CIRA-86 includes monthly and zonally mean temperatures and pressures (0–120 km) with almost global coverage (80°N – 80°S) at an interval of 10° . We averaged the two temperature data at 30°N and 40°N for CEC, and used the temperature data at 30°N for ECS. The mixing ratios of ozone and water vapor at pressures less than 0.01 hPa

were assumed to be equal to those at the upper boundary (0.01 hPa) of the MERRA data because there are no appropriate data to refer. We confirmed that the effects of the assumption in the upper vertical range were negligibly small for our calculation.

The information on surface albedo for simulating UV radiance spectra was taken from the database described by Kleipool et al. (2008). This database contains the monthly global maps of the Earth's surface Lambertian equivalent reflectance (LER) deduced from the Aura/OMI measurements. We assumed that surface albedo was constant in the selected UV ranges (305–340 nm). We obtained monthly and spatially averaged albedo values of 0.056 (June) and 0.063 (December) for CEC and 0.065 (June) and 0.084 (December) for ECS, respectively, from the LER data at the wavelength of 328.1 nm, which is the shortest wavelength in the database. The impact of the uncertainty of the UV surface albedo on tropospheric ozone measurements from space was discussed in Noguchi et al. (2014). The surface emissivity for modeling the TIR radiance spectra was estimated by linear regression analysis based on the Advanced Space-borne Thermal Emission Reflection Radiometer (ASTER) Spectral Library (Baldrige et al., 2009). The surface emissivity for MW was set to 1.0 for the entire range. MW limb measurements are generally insensitive to the surface emissivity since the atmosphere is strongly opaque in this wavelength range.

3 Synergetic retrieval simulation

3.1 Forward models of UV, TIR, and MW regions

We used the SCIATRAN radiative transfer model version 3.1 (Rozañov et al., 2005), the Line-By-Line Radiative Transfer Model (LBLRTM) version 12.1 (Clough et al., 2005), and the Advanced Model for Atmospheric Terahertz Radiation Analysis and Simulation (AMATERASU) (Baron et al., 2008) for the calculation of spectra in the UV, TIR, and MW wavelength ranges, respectively. In the presented study, no bias is assumed between the three forward models in order to investigate potential advantage of including MW observation to retrieval of tropospheric ozone.

The SCIATRAN model was developed by the Institute of Remote Sensing/Institute of Environmental Physics (IFE/IUP) of the University of Bremen, Germany, for fast and precise simulation of radiance spectra in the UV, VIS and Near Infrared ranges as measured by spaceborne instruments, e.g., GOME (240–790 nm) and SCIAMACHY (240–2400 nm). SCIATRAN is applicable to spectral regions ranging from 175.44 nm to 2400 nm, and is basically compatible with arbitrary observation geometries and sensor positions in space, in the atmosphere, and on the ground. The spherical shape of the Earth's atmosphere, including the refraction effect, is properly taken into account when simulating the radiance spectra.

The LBLRTM model is an accurate and efficient line-by-line radiative transfer model, and it has been extensively validated for atmospheric radiance spectra from UV to submillimeter-wave ranges. The line-by-line calculation of the optical thickness of the atmospheric layers is conducted on the basis of the spectroscopic line parameter database (HITRAN 2008) with its updates (Rothman et al., 2009). This model is used as the forward model in retrieval algorithms for analyzing spaceborne measurements such as EOS-Aura/TES (Clough et al., 2006), and GOSAT/TANSO-FTS (Saitoh et al., 2009).

The AMATERASU model consists of a line-by-line radiative transfer calculation allowing for a multi-layered horizontally homogeneous shell atmosphere. This model has been implemented in the retrieval analysis of the SMILES measurements (e.g., Baron et al., 2011) and in the feasibility study of a submillimeter instrument for planetary science (Kasai et al., 2012).

The spectroscopic parameters are from commonly used databases such as HITRAN 2008 (Rothman et al., 2009) and the JPL spectroscopic catalog (Pickett et al., 1998). The continuum absorption due to dry and wet air are also included and are based on the formulation in Pardo et al. (2001).

3.2 Theoretical retrieval basis and error estimation

- 5 The optimal estimation method (OEM) (Rodgers, 2000) was used for the synergetic retrieval system and their error estimations. The retrieved state vector $\hat{\mathbf{x}}$ was estimated by minimizing the differences between the observed radiance spectra \mathbf{y}_{obs} and the modeled radiance spectra \mathbf{y}_{mod} , using a constraint from an a priori state vector \mathbf{x}_a .

$$\hat{\mathbf{x}} = A\mathbf{x} + (I - A)\mathbf{x}_a + G\boldsymbol{\epsilon} \quad (1)$$

- In this equation, \mathbf{x} is the true state vector, A is the averaging kernel matrix, G is the gain (contribution function) matrix, and $\boldsymbol{\epsilon}$ is the measurement noise vector. The averaging kernel matrix characterizing the sensitivity of the retrieved state vector $\hat{\mathbf{x}}$ to the true state vector \mathbf{x} is given by

$$A = \frac{\partial \hat{\mathbf{x}}}{\partial \mathbf{x}} = GK = (K^T S_\epsilon^{-1} K + S_a^{-1})^{-1} K^T S_\epsilon^{-1} K, \quad (2)$$

- where S_a and S_ϵ are the a priori covariance matrix and the measurement error covariance matrix, respectively. K is a weighting function matrix ($K = \partial \mathbf{y}_{\text{mod}} / \partial \mathbf{x}$). A corresponds to the identity matrix when the retrieved profile is equal to the true atmospheric profile. The number of state vector elements which are independently resolved is obtained by summation of diagonal elements of A , and is defined as DFS. The i th element of measurement response vector, $\mathbf{m}[i]$, is defined as

$$\mathbf{m}[i] = \sum_j A[i, j]. \quad (3)$$

A value of the measurement response element near unity indicates that almost all information in the retrieval result comes from the observation spectra, while a small value indicates that the retrieval result is largely influenced by the a priori.

- 20 The total retrieval error covariance \hat{S} is calculated using the covariance matrices of the smoothing error S_s and measurement noise S_m .

$$\begin{aligned} \hat{S} &= S_s + S_m \\ &= (I - A) S_a (I - A)^T + G S_\epsilon G^T \\ &= (K^T S_\epsilon^{-1} K + S_a^{-1})^{-1} \end{aligned} \quad (4)$$

- 25 The square root of the \hat{S} diagonals is the total retrieval error in $\hat{\mathbf{x}}$ ($\boldsymbol{\epsilon}_x$). The value of $\boldsymbol{\epsilon}_x$ at i th layer is given by

$$\boldsymbol{\epsilon}_x[i] = \sqrt{\hat{S}[i, i]}. \quad (5)$$

We evaluated the sensitivity of the vertical profile of ozone from the synergetic retrieval for seven different combinations of the wavelength ranges, i.e., UV, TIR, MW, TIR+MW, UV+MW, UV+TIR and UV+TIR+MW, in the 20 atmospheric

scenarios. The state vectors \mathbf{x} , $\hat{\mathbf{x}}$ and \mathbf{x}_a were calculated using logarithm units of the volume mixing ratio (VMR). The diagonal components of S_a were the squares of the a priori error σ_a (100 % of the log-based VMR) at each vertical pressure grid). The diagonal components of S_ϵ were the squares of the measurement error σ_ϵ . The off-diagonal components of S_a and S_ϵ were set to zero.

- 5 We normalized the state vector \mathbf{x} and measurement vector \mathbf{y} with σ_a and σ_ϵ because values with different order in a vector and a matrix often cause undesirable mathematical errors in computational calculation.

$$\mathbf{u} = \frac{\mathbf{x} - \mathbf{x}_a}{\sigma_a} \quad (6)$$

$$\mathbf{v} = \frac{\mathbf{y}_{\text{obs}} - \mathbf{y}_{\text{mod}}}{\sigma_\epsilon} \quad (7)$$

The normalized weighting function was given by

$$10 \quad K' = KD(\sigma_a/\sigma_\epsilon). \quad (8)$$

Here, $D(\mathbf{a})$ is a diagonal matrix whose diagonal elements are equal to the components of the vector \mathbf{a} . S_a and S_ϵ were normalized in the same way.

$$S'_a = D(1/\sigma_a)S_aD(1/\sigma_a)^T \quad (9)$$

$$S'_\epsilon = D(1/\sigma_\epsilon)S_\epsilon D(1/\sigma_\epsilon)^T \quad (10)$$

- 15 Using the normalized vectors and matrices, A and \hat{S} are expressed as

$$A = \left(K'^T S'_\epsilon^{-1} K' + S'_a^{-1} \right)^{-1} K'^T S'_\epsilon^{-1} K', \quad (11)$$

$$\hat{S} = \left(K'^T S'_\epsilon^{-1} K' + S'_a^{-1} \right)^{-1}. \quad (12)$$

We evaluated the sensitivity of ozone retrieval for seven wavelength combinations in terms of the DFS and partial column error (PCE). We calculated DFS and PCE for the UT, MT and LMT regions as follows. The value of DFS from the i_{min} th

- 20 vertical layer to the i_{max} th layer is given by

$$\text{DFS} = \sum_{i=i_{\text{min}}}^{i_{\text{max}}} A[i, i]. \quad (13)$$

The ozone partial column (PC) for the same vertical layers is defined as

$$\text{PC} = \sum_{i=i_{\text{min}}}^{i_{\text{max}}} \frac{p[i] \cdot \text{VMR}[i]}{k_B \cdot T[i]} \Delta z[i]. \quad (14)$$

- Here, $p[i]$, $\text{VMR}[i]$, $T[i]$ and $\Delta z[i]$ are pressure, VMR of ozone, temperature, and the vertical length of the i th layer, respectively. k_B is the Boltzmann constant. We defined partial column error, PCE, as the relative error in PC by

$$\text{PCE} = \frac{1}{\text{PC}} \sum_{i=i_{\text{min}}}^{i_{\text{max}}} \frac{p[i] \cdot \epsilon_{\text{VMR}}[i]}{k_B \cdot T[i]} \Delta z[i]. \quad (15)$$

$\epsilon_{\text{VMR}}[i]$ is the total retrieval error in ozone VMR at the i th layer.

4 Results and discussion

The sensitivity of ozone retrieval for the UT (215–383 hPa), MT (383–749 hPa), and LMT (>749 hPa) regions was investigated in terms of DFS. The left column of Fig. 3 shows the DFS values calculated with Eq. (13) for the seven wavelength combinations: UV alone, TIR alone, MW alone, TIR+MW, UV+MW, UV+TIR and UV+TIR+MW. The DFS values were averaged in June in CEC (shown by red markers in Fig. 3), June in ECS (purple), December in CEC (green), December in ECS (blue) and all 20 profiles (black). The error bar represents the standard deviation.

The DFS value in the UT region averaged for all 20 profiles was calculated to be 0.16 ± 0.08 , 0.59 ± 0.10 and 0.44 ± 0.41 for the UV, TIR, and MW wavelength range, respectively. None of the DFS average values for one wavelength range was larger than unity. Using more than one wavelength range, the DFS value increased to 1.15 ± 0.25 , 0.90 ± 0.30 , 0.62 ± 0.08 , and 1.21 ± 0.28 , for the wavelength combinations of TIR+MW, UV+MW, UV+TIR, and UV+TIR+MW, respectively. The DFS of the UV+TIR combination was the lowest among those of more than one wavelength range, and adding the MW region increased the value by about two times. The additional MW region was hence most effective at improving the retrieval of ozone in the UT region.

In the MT region, the TIR measurements are the main contributors of DFS information. The DFS values were 0.50 ± 0.16 , 0.83 ± 0.11 , and less than 0.01 for the UV, TIR and MW wavelength ranges, respectively. The DFS values increased in the same way as in the UT calculation by adding measurements in different wavelength ranges. The average DFS values of the 20 profiles were 1.03 ± 0.09 , 0.73 ± 0.09 , 1.00 ± 0.09 and 1.23 ± 0.13 for TIR+MW, UV+MW, UV+TIR and UV+TIR+MW, respectively. It should be noted that the MW measurements, which have no information on ozone in the MT region because of atmospheric opacity, certainly increased the DFS value in the MT region from 1.00 in the TIR+UV measurements to 1.23 (about a 20 % increase). This indicates that the information on ozone in the stratosphere and UT, where the sensitivity of MW is high, is also important for retrieval of ozone in the MT region.

The DFS values in the LMT region were generally smaller than those in the MT and LT regions. They were calculated to be 0.20 ± 0.13 , 0.21 ± 0.15 , less than 0.01, 0.20 ± 0.14 , 0.26 ± 0.15 , 0.46 ± 0.25 and 0.60 ± 0.27 for UV, TIR, MW, TIR+MW, UV+MW, UV+TIR and UV+TIR+MW, respectively. The DFS values of the UV and TIR wavelength ranges were almost the same, while the MW measurements had no sensitivity in the LMT region. Similar to the MT region, the DFS values of the UV+TIR measurements (0.46) increased to 0.60 (about a 40 % increase) as a result of adding the MW measurement.

The relative error in the partial column of ozone, PCE, calculated using Eq. (15), is shown in the right column of Fig. 3. PCE generally decreased when more wavelength regions were used. PCE was approximately 55–70 % in the LMT, MT and UT regions. PCE for the MW measurements alone could not be estimated in the MT and LMT because the DFS values were almost zero and there was no sensitivity with which to retrieve the ozone amount from the MW measurements.

The sensitivity of MW measurement in the UT region largely depended on the atmospheric profile used in this simulation, and its dependency transferred to the wavelength combinations including the MW measurement. The DFS values of the MW measurement in the UT region for profiles in December 2009 (green and blue markers in Fig. 3) were larger than those in June 2009 (red and purple markers). The sensitivity of the MW measurements in the UT region increased for profiles with

large amounts of ozone in the UT region. In the LMT, the DFS values of the UV and TIR measurements strongly depended on the atmospheric profiles. The average value of the partial column of ozone in the LMT region at CEC in June 2009 was $5.03 \times 10^{21} \text{ m}^{-2}$, the largest among the four cases. Only the DFS value of UV+TIR+MW at CEC in June 2009 (red marker) was larger than unity (1.03 ± 0.01). This shows that retrieval combining UV, TIR and MW measurements can possibly retrieve
5 the ozone amount in the LMT region with a DFS value of unity when the LMT ozone is enhanced as large as approximately $5 \times 10^{21} \text{ m}^{-2}$.

More details of the vertical characteristics are discussed with A . Figures 4 and 5 show A and m obtained from the simulation using the atmospheric profile #01 and #12 for all of the wavelength combinations. The DFS values in the LMT for the UV+TIR+MW measurements of profiles #01 and #12 were respectively estimated to be 1.04 and 0.27, i.e., which were the
10 highest and lowest values among the 20 profiles. In the case of profile #01, the UV, TIR and MW measurements provided information in the LMT, MT to UT, and UT to the stratosphere, respectively. The UV and TIR measurements were important to retrieve the ozone amount in the LMT when only one wavelength range was used because their peaks in the row of A were located in the LMT region. The FWHM of the row of A of the UV and TIR measurements in the LMT was approximately 3 km. The peak value in the row of A increased from 0.25 of the UV and TIR measurements to 0.35 as a result of adding the two
15 measurements. The combination of TIR and UV improved the sensitivity of retrieval of ozone in the LMT, as shown in Worden et al. (2007) and Natraj et al. (2011). Adding the MW measurement further increased it to 0.4. In profile #12 (less ozone in the LMT), the peak of the row of A for the UV measurement was located in the MT (maximum value of 0.1). Although the peak value in the MT increased to 0.23 as a result of adding the TIR and MW measurements, the peak value in the LMT remained low.

20 As a whole, it was shown that retrieval of ozone in the LMT was improved by adding the MW limb measurements to the UV and TIR nadir measurements. When ozone is enhanced in the LMT and also the averaging kernel matrices of UV and TIR measurements have their peaks in this region, it may be possible to retrieve the ozone in the LMT with a DFS value of more than unity.

5 Conclusions

25 We performed a feasibility study of obtaining a vertically resolved ozone profile in the troposphere from synergetic retrieval using a combination of three separate wavelength ranges (UV, TIR, and MW). Observation geometries used in this study were the nadirs for the UV and TIR measurements and limb for the MW measurement from low orbit at a height of 300 km (the height of the ISS). Twenty atmospheric profiles at CEC and ECS in June and December 2009 were used for the simulation. We evaluated the sensitivities of retrieval of ozone in the three vertical regions (UT (215–383 hPa), MT (383–749 hPa) and LMT
30 (>749 hPa)) in terms of the DFS, PCE and A based on the OEM calculation.

The TIR measurement was most sensitive for retrieving ozone in the UT when only one wavelength range was used. The additional MW measurement was most effective at improving the sensitivity in the UT when combining several wavelength ranges. Adding the MW measurement to the UV+TIR measurements increased the DFS value in the UT by a factor of two. In

the MT region, the contribution of the TIR measurement was dominant in the DFS calculation. The average DFS value of the TIR measurement for all of the 20 profiles used in this study was 0.83 ± 0.11 . It increased to more than unity by adding either the UV or MW measurements. The UV and TIR measurements were dominant in the retrieval of ozone in the LMT region. The DFS value in the LMT strongly depended on the ozone abundance. Our calculation shows that the combination of UV, TIR and MW measurements is able to retrieve the ozone abundance in the LMT with a DFS value larger than unity, when the ozone abundance is as high as approximately $5 \times 10^{21} \text{ m}^{-2}$ in the LMT and the peak of A is in the LMT for both the UV and TIR measurements.

It is worth noting that adding MW measurements to the UV and TIR measurement combinations improved sensitivity not only in the UT but also in the MT and LMT; nevertheless, less information on ozone in the MT and LMT was derived from the MW measurement alone. The DFS values increased by 95 %, 23 % and 40 % in the UT, MT and LMT by adding the MW measurements to the UV+TIR measurements. This indicates that reducing the uncertainty of ozone abundance in the stratosphere is important for estimating an accurate tropospheric ozone profile.

Acknowledgements. This work was supported by the Funding Program for Next Generation World-Leading Researchers (NEXT Program) (No. GR101). This research was partly supported by Coordination Funds for Promoting Space Utilization by the Ministry of Education, Culture, Sports, Science and Technology (MEXT), Japan. We are grateful to Dr. K. Takigawa for providing us with his numerical simulation data for this study. The MERRA data used in this study was provided by the Global Modeling and Assimilation Office (GMAO) at NASA Goddard Space Flight Center through the NASA GES DISC online archive. We made use of CIRA-86. We thank Dr. K. Kikuchi for discussing with us the specifications of the MW instrument proposed for the Air Pollution Observations from the ISS. We thank our colleagues in the Aura MLS team (JPL) for valuable discussion on the frequency selection of the APOLLO MW instrument. We are grateful to Dr. A. Rozanov for giving a lot of useful comments of SCIATRAN.

References

- Baldrige, A. M., Hook, S. J., Grove, C. I., and Rivera, G.: The ASTER spectral library version 2.0, *Remote Sensing of Environment*, 113, 711–715, 2009.
- Baron, P., Mendrok, J., Kasai, Y., Ochiai, S., Seta, T., Sagi, K., Suzuki, K., Sagawa, H., and Urban, J.: AMATERAU: Model for atmospheric
5 terahertz radiation analysis and simulation, *Journal of National Institute of Information and Communications Technology*, 55, 109–121, 2008.
- Baron, P., Urban, J., Sagawa, H., Möller, J., Murtagh, D. P., Mendrok, J., Dupuy, E., Sato, T. O., Ochiai, S., Suzuki, K., Manabe, T., Nishibori, T., Kikuchi, K., Sato, R., Takayanagi, M., Murayama, Y., Shiotani, M., and Kasai, Y.: The Level 2 research product algorithms for the Superconducting Submillimeter-Wave Limb-Emission Sounder (SMILES), *Atmospheric Measurement Techniques*, 4, 2105–2124,
10 doi:10.5194/amt-4-2105-2011, 2011.
- Boynard, A., Clerbaux, C., Coheur, P. F., Hurtmans, D., Turquety, S., George, M., Hadji-Lazaro, J., Keim, C., and Meyer-Arneck, J.: Measurements of total and tropospheric ozone from IASI: comparison with correlative satellite, ground-based and ozonesonde observations, *Atmospheric chemistry and physics*, 9, 6255–6271, 2009.
- Brinksma, E. J., Bracher, A., Lolkema, D. E., Segers, A. J., Boyd, I. S., Bramstedt, K., Claude, H., Godin-Beekmann, S., Hansen, G., Kopp,
15 G., Leblanc, T., McDermid, I. S., Meijer, Y. J., Nakane, H., Parrish, A., von Savigny, C., Stebel, K., Swart, D. P. J., Taha, G. and Piters, A. J. M.: Geophysical validation of SCIAMACHY limb ozone profiles, *Atmospheric Chemistry and Physics*, 6, 197–209, 2006.
- Clerbaux, C., Boynard, A., Clarisse, L., George, M., Hadji-Lazaro, J., Herbin, H., Hurtmans, D., Pommier, M., Razavi, A., Turquety, S., Wespes, C. and Coheur, P. F.: Monitoring of atmospheric composition using the thermal infrared IASI/MetOp sounder, *Atmospheric Chemistry and Physics*, 9, 6041–6054, 2009.
- 20 Clough, S. A., Shephard, M. W., Mlawer, E. J., Delamere, J. S., Iacono, M. J., Cady-Pereira, K., Boukabara, S., and Brown, P. D.: Atmospheric radiative transfer modeling: a summary of the AER codes, *Journal of Quantitative Spectroscopy and Radiative Transfer*, 91, 233–244, 2005.
- Clough, S. A., Shephard, M. W., Worden, J., Brown, P. D., Worden, H. M., Luo, M., Rodgers, C. D., Rinsland, C. P., Goldman, A., Brown, L., Kulawik, S. S., Eldering, A., Lampel, M., Osterman, G., Beer, R., Bowman, K., Cady-Pereira, K. E., and Mlawer, E. J.: Forward model
25 and Jacobians for tropospheric emission spectrometer retrievals, *IEEE Transactions on Geoscience and Remote Sensing*, 44, 1308–1323, 2006.
- Cuesta, J., Eremenko, M., Liu, X., Dufour, G., Cai, Z., Höpfner, M., von Clarmann, T., Sellitto, P., Forêt, G., Gaubert, B., Beekmann, M., Orphal, J., Chance, K., Spurr, R., and Flaud, J. M.: Satellite observation of lowermost tropospheric ozone by multispectral synergism of IASI thermal infrared and GOME-2 ultraviolet measurements over Europe, *Atmospheric Chemistry and Physics*, 13, 9675–9693, 2013.
- 30 Dentener, F., Keating, T., and Akimoto, H.: Hemispheric transport of air pollution, United Nations, ISBN, pp. 978–992, 2010.
- Fleming, E. L., Chandra, S., Barnett, J. J., and Corney, M.: Zonal mean temperature, pressure, zonal wind and geopotential height as functions of latitude, *Advances in Space Research*, 10, 11–59, 1990.
- Fu, D., Worden, J. R., Liu, X., Kulawik, S. S., Bowman, K. W., and Natraj, V.: Characterization of ozone profiles derived from Aura TES and OMI radiances, *Atmospheric Chemistry and Physics*, 13, 3445–3462, 2013.
- 35 Fujinawa, T., Kasai, Y., Mahani, M., uvSCOPE team and APOLLO mission team: Japanese future mission for air quality uvSCOPE and APOLLO, 8th Atmospheric Limb workshop Abstracts, 2015.

- Grell, G. A., Peckham, S. E., Schmitz, R., McKeen, S. A., Frost, G., Skamarock, W. C. and Eder, B.: Fully coupled "online" chemistry within the WRF model, *Atmospheric Environment*, 39, 6957–6975, 2005.
- Hess, M., Koepke, P., and Schult, I.: Optical properties of aerosols and clouds: The software package OPAC, *Bulletin of the American meteorological society*, 79, 831–844, 1998.
- 5 Kasai, Y., Kita, K., Kanaya, Y., Gmap-Asia and Apollo Mission Team: The Japanese Air Pollution Observation Missions, GMAP-Asia and APOLLO, AGU Fall Meeting Abstracts, 2011.
- Kasai, Y., Sagawa, H., Kuroda, T., Manabe, T., Ochiai, S., Kikuchi, K., Nishibori, T., Baron, P., Mendrok, J., Hartogh, P., Murtagh, D., Urban, J., von Schéele, F., and Frisk, U.: Overview of the Martian atmospheric submillimetre sounder FIRE, *Planetary and Space Science*, 63, 62–82, 2012.
- 10 Kikuchi, K., Nishibori, T., Ochiai, S., Ozeki, H., Irimajiri, Y., Kasai, Y., Koike, M., Manabe, T., Mizukoshi, K., Murayama, Y., Nagahama, T., Sano, T., Sato, R., Seta, M., Takahashi, C., Takayanagi, M., Masuko, H., Inatani, J., Suzuki, M., and Shiotani, M.: Overview and early results of the Superconducting Submillimeter-Wave Limb-Emission Sounder (SMILES), *Journal of Geophysical Research: Atmospheres*, 115, D23306, doi:10.1029/2010JD014379, 2010.
- Kleipool, Q. L., Dobber, M. R., de Haan, J. F., and Levelt, P. F.: Earth surface reflectance climatology from 3 years of OMI data, *Journal of*
- 15 *Geophysical Research: Atmospheres*, 113, 2008.
- Kyrölä, E., Tamminen, J., Leppelmeier, G. W., Sofieva, V., Hassinen, S., Bertaux, J. L., Hauchecorne, A., Dalaudier, F., Cot, C., Korabely, O., Fanton d'Andon, O., Barrot, G., Mangin, A., Théodore, B., Guirlet, M., Etanchaud, F., Snoeij, P., Koopman, R., Saavedra, L., Fraisse, R., Fussen, D. and Vanhellefont, F.: GOMOS on Envisat: An overview, *Advances in Space Research*, 33, 1020–1028, 2004.
- Landgraf, J., and Hasekamp, O. P.: Retrieval of tropospheric ozone: The synergistic use of thermal infrared emission and ultraviolet reflectivity measurements from space, *Journal of Geophysical Research: Atmospheres*, 112, 2007.
- 20 Levelt, P. F., van den Oord, G. H. J., Dobber, M. R., Malkki, A., Visser, H., de Vries, J., Stammes, P., Lundell, J. O. V., and Saari, H.: The ozone monitoring instrument, *IEEE Transactions on geoscience and remote sensing*, 44, 1093–1101, 2006.
- Munro, R., Eisinger, M., Anderson, C., Callies, J., Corpaccioli, E., Lang, R., Lefebvre, A., Livschitz, Y., and Albinana, A. P.: GOME-2 on MetOp, in: *Proc. of The 2006 EUMETSAT Meteorological Satellite Conference*, Helsinki, Finland, pp. 12–16, 2006.
- 25 Natraj, V., Liu, X., Kulawik, S., Chance, K., Chatfield, R., Edwards, D. P., Eldering, A., Francis, G., Kurosu, T., Pickering, K., Spurr, R. and Worden, H.: Multi-spectral sensitivity studies for the retrieval of tropospheric and lowermost tropospheric ozone from simulated clear-sky GEO-CAPE measurements, *Atmospheric Environment*, 45, 7151–7165, 2011.
- Noguchi, K., Richter, A., Rozanov, V., Rozanov, A., Burrows, J. P., Irie, H., and Kita, K.: Effect of surface BRDF of various land cover types on geostationary observations of tropospheric NO₂, *Atmospheric Measurement Techniques*, 7, 3497–3508, 2014.
- 30 Osterman, G. B., Kulawik, S. S., Worden, H. M., Richards, N. A. D., Fisher, B. M., Eldering, A., Shephard, M. W., Froidevaux, L., Labow, G., Luo, M., Herman, R. L., Bowman, K. W., and Thompson, A. M.: Validation of Tropospheric Emission Spectrometer (TES) measurements of the total, stratospheric, and tropospheric column abundance of ozone, *Journal of Geophysical Research: Atmospheres*, 113, 2008.
- Pardo, J. R., Serabyn, E., and Cernicharo, J.: Submillimeter atmospheric transmission measurements on Mauna Kea during extremely dry El Niño conditions: Implications for broadband opacity contributions, *Journal of Quantitative Spectroscopy and Radiative Transfer*, 68,
- 35 419–433, 2001.
- Pickett, H. M., Poynter, R. L., Cohen, E. A., Delitsky, M. L., Pearson, J. C., and Müller, H. S. P.: Submillimeter, millimeter and microwave spectral line catalog, *Journal of Quantitative Spectroscopy and Radiative Transfer*, 60, 883–890, doi:10.1016/S0022-4073(98)00091-0, 1998.

- Rienecker, M. M., Suarez, M. J., Gelaro, R., Todling, R., Bacmeister, J., Liu, E., Bosilovich, M. G., Schubert, S. D., Takacs, L., Kim, G. K., Bloom, S., Chen, J., Collins, D., Conaty, A., da Silva, A., Gu, W., Joiner, J., Koster, R. D., Lucchesi, R., Molod, A., Owens, T., Pawson, S., Pegion, P., Redder, C. R., Reichle, R., Robertson, F. R., Ruddick, A. G., Sienkiewicz, M., and Woollen, J.: MERRA: NASA's modern-era retrospective analysis for research and applications, *Journal of Climate*, 24, 3624–3648, 2011.
- 5 Rodgers, C. D.: *Inverse methods for atmospheric sounding: Theory and practice*, Series on Atmospheric, Oceanic and Planetary Physics, World Scientific, 2, 3605–3609, 2000.
- Rothman, L. S., Gordon, I. E., Barbe, A., Benner, D. C., Bernath, P. F., Birk, M., Boudon, V., Brown, L. R., Campargue, A., Champion, J. P., Chance, K., Coudert, L. H., Dana, V., Devi, V. M., Fally, S., Flaud, J. M., Gamache, R. R., Goldman, A., Jacquemart, D., Kleiner, I., Lacombe, N., Lafferty, W. J., Mandin, J. Y., Massie, S. T., Mikhailenko, S. N., Miller, C. E., Moazzen-Ahmadi, N., Naumenko, O. V.,
- 10 Nikitin, A. V., Orphal, J., Perevalov, V. I., Perrin, A., Predoi-Cross, A., Rinsland, C. P., Rotger, M., Šimečková, M., Smith, M. A. H., Sung, K., Tashkun, S. A., Tennyson, J., Toth, R. A., Vandaele, A. C., and Vander Auwera, J.: The HITRAN 2008 molecular spectroscopic database, *Journal of Quantitative Spectroscopy and Radiative Transfer*, 110, 533–572, doi:10.1016/j.jqsrt.2009.02.013, 2009.
- Roazanov, A., Roazanov, V., Buchwitz, M., Kokhanovsky, A., and Burrows, J. P.: SCIATRAN 2.0—A new radiative transfer model for geophysical applications in the 175–2400 nm spectral region, *Advances in Space Research*, 36, 1015–1019, 2005.
- 15 Saitoh, N., Imasu, R., Ota, Y., and Niwa, Y.: CO₂ retrieval algorithm for the thermal infrared spectra of the Greenhouse Gases Observing Satellite: Potential of retrieving CO₂ vertical profile from high-resolution FTS sensor, *Journal of Geophysical Research: Atmospheres*, 114, 2009.
- Sellitto, P., Del Frate, F., Solimini, D., and Casadio, S.: Tropospheric ozone column retrieval from ESA-Envisat SCIAMACHY nadir UV/VIS radiance measurements by means of a neural network algorithm, *IEEE Transactions on Geoscience and Remote Sensing*, 50, 998–1011, doi:10.1109/TGRS.2011.2163198, 2012a.
- 20 Sellitto, P., Di Noia, A., Del Frate, F., Burini, A., Casadio, S., and Solimini, D.: On the role of visible radiation in ozone profile retrieval from nadir UV/VIS satellite measurements: An experiment with neural network algorithms inverting SCIAMACHY data, *Journal of Quantitative Spectroscopy and Radiative Transfer*, 113, 1429–1436, doi:10.1016/j.jqsrt.2012.04.007, 2012b.
- Sudo, K., Takahashi, M., Kurokawa, J., and Akimoto, H.: CHASER: A global chemical model of the troposphere 1. Model description, *Journal of Geophysical Research: Atmospheres*, 107, 2002.
- 25 Takigawa, M., Niwano, M., Akimoto, H., and Takahashi, M.: Development of a one-way nested global-regional air quality forecasting model, *Sola*, 3, 81–84, 2007.
- Takigawa, M., Niwano, M., Akimoto, H., Takahashi, M., and Kobayashi, K.: Projection of surface ozone over East Asia in 2020, *Journal of Agriculture Meteorology*, 65, 161–166, 2009.
- 30 Urban, J., Lautié, N., Le Flochmoën, E., Jiménez, C., Eriksson, P., de La Noë, J., Dupuy, E., Ekström, M., El Amraoui, L., Frisk, U., Murtagh, D., Olberg, M., and Ricaud, P.: Odin/SMR limb observations of stratospheric trace gases: Level 2 processing of ClO, N₂O, HNO₃, and O₃, *Journal of Geophysical Research: Atmospheres*, 110, 2005.
- Waters, J. W., Froidevaux, L., Harwood, R. S., Jarnot, R. F., Pickett, H. M., Read, W. G., Siegel, P. H., Cofield, R. E., Filipiak, M. J., Flower, D. A., Holden, J. R., Lau, G. K., Livesey, N. J., Manney, G. L., Pumphrey, H. C., Santee, M. L., Wu, D. L., Cuddy, D. T., Lay, R. R., Loo, M. S., Perun, V. S., Schwartz, M. J., Stek, P. C., Thurstans, R. P., Boyles, M. A., Chandra, K. M., Chavez, M. C., Chen, G. S., Chudasama, B. V., Dodge, R., Fuller, R. A., Girard, M. A., Jiang, J. H., Jiang, Y., Knosp, B. W., LaBelle, R. C., Lam, J. C., Lee, K. A., Miller, D., Oswald, J. E., Patel, N. C., Pukala, D. M., Quintero, O., Scaff, D. M., Snyder, W. V., Tope, M. C., Wagner, P. A., and Walch, M. J.:

The earth observing system microwave limb sounder (EOS MLS) on the Aura satellite, *IEEE Transactions on Geoscience and Remote Sensing*, 44, 1075–1092, 2006.

WHO: Burden of disease from Ambient Air Pollution for 2012, Geneva: World Health Organization, 2014.

Worden, J., Liu, X., Bowman, K., Chance, K., Beer, R., Eldering, A., Gunson, M., and Worden, H.: Improved tropospheric ozone profile retrievals using OMI and TES radiances, *Geophysical Research Letters*, 34, 2007.

Ziemke, J. R., Chandra, S., Duncan, B. N., Froidevaux, L., Bhartia, P. K., Levelt, P. F., and Waters, J. W.: Tropospheric ozone determined from Aura OMI and MLS: Evaluation of measurements and comparison with the Global Modeling Initiative's Chemical Transport Model, *Journal of Geophysical Research: Atmospheres*, 111, 2006.

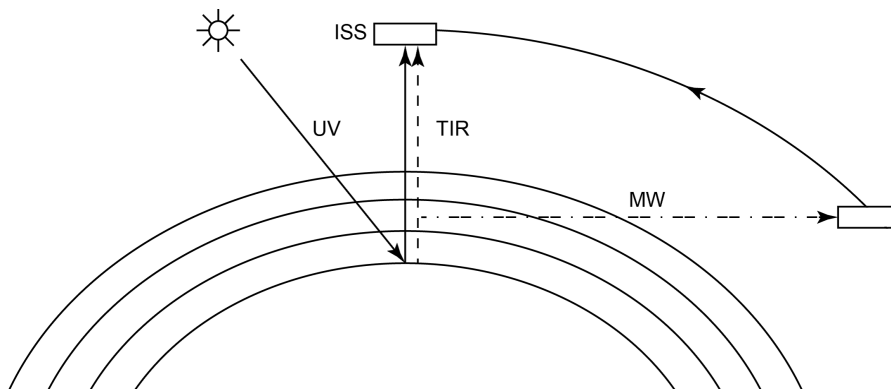


Figure 1. Geometries of down-looking nadir (UV and TIR) and limb (MW) observations.

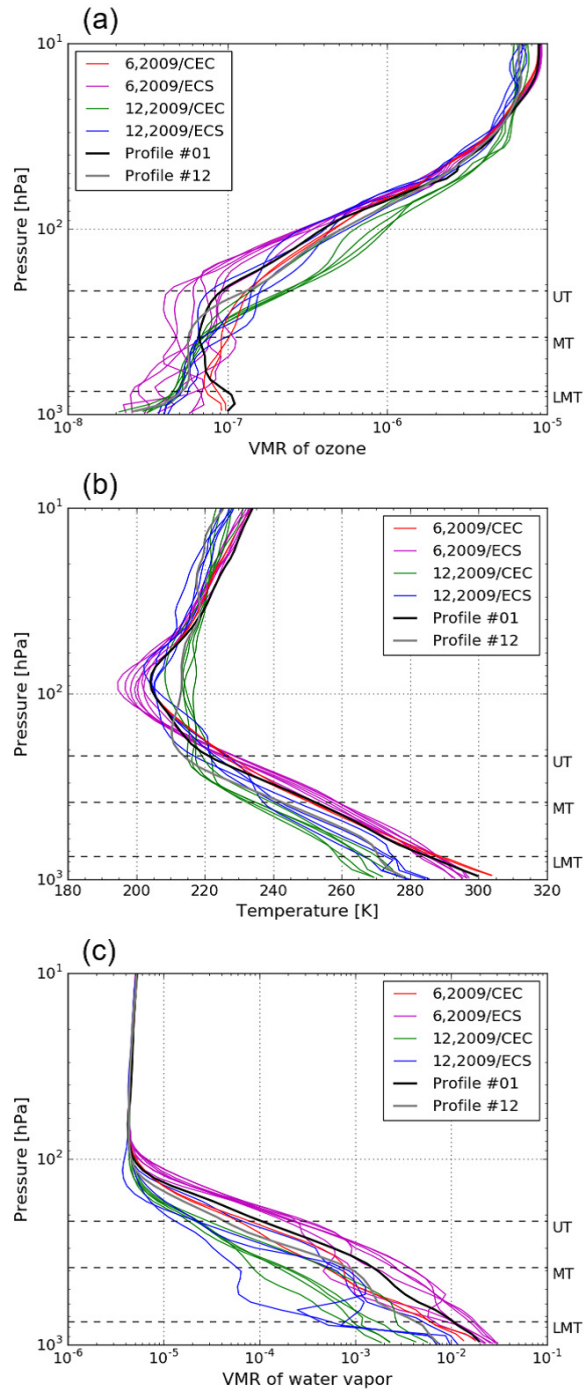


Figure 2. The 20 atmospheric scenarios used in this study: (a) VMR of ozone, (b) temperature, and (c) VMR of water vapor. These atmospheric scenarios can be divided into four groups, as denoted by four different color curves: (red) June 2009 in CEC, (purple) June 2009 in ECS, (green) December 2009 in CEC, and (blue) December 2009 in ECS. Two example profiles #01 and #12, represented by the black and gray lines, respectively, are the ones used to obtain the results shown in Figs. 4 and 5.

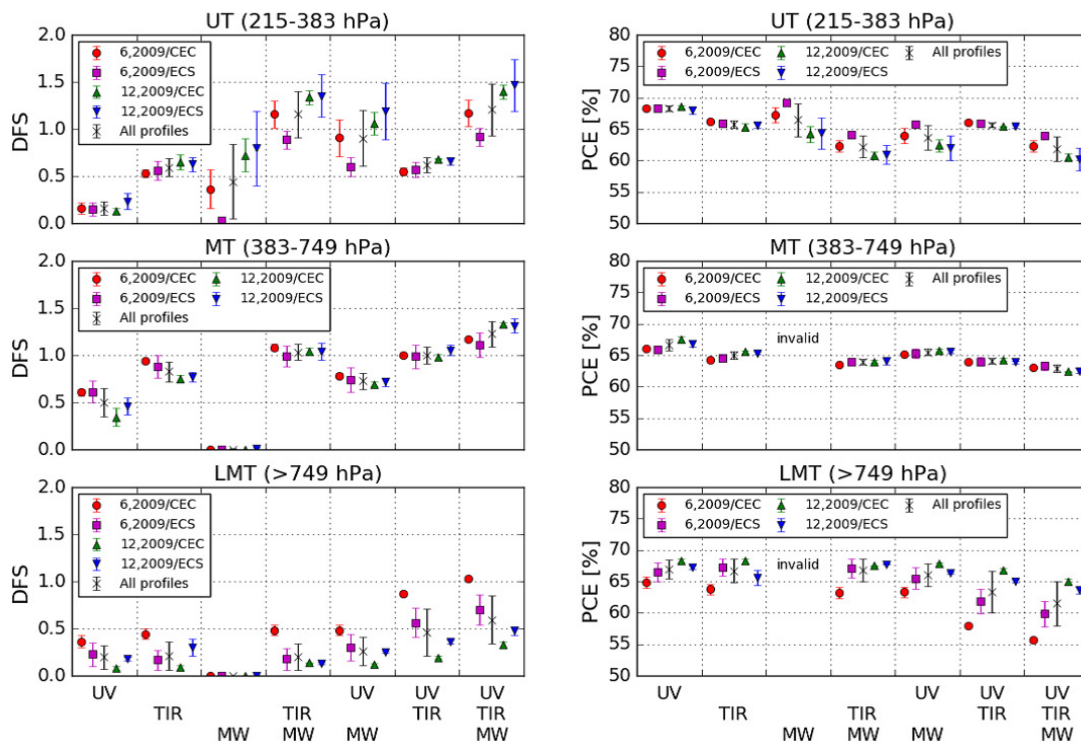


Figure 3. Values of DFS and PCE in the upper troposphere (UT, 215–383 hPa), middle troposphere (MT, 383–749 hPa), and lowermost troposphere (LMT, >749 hPa): (red) June 2009 in CEC, (purple) June 2009 in ECS, (green) December 2009 in CEC, (blue) December 2009 in ECS and (black) all of 20 profiles.

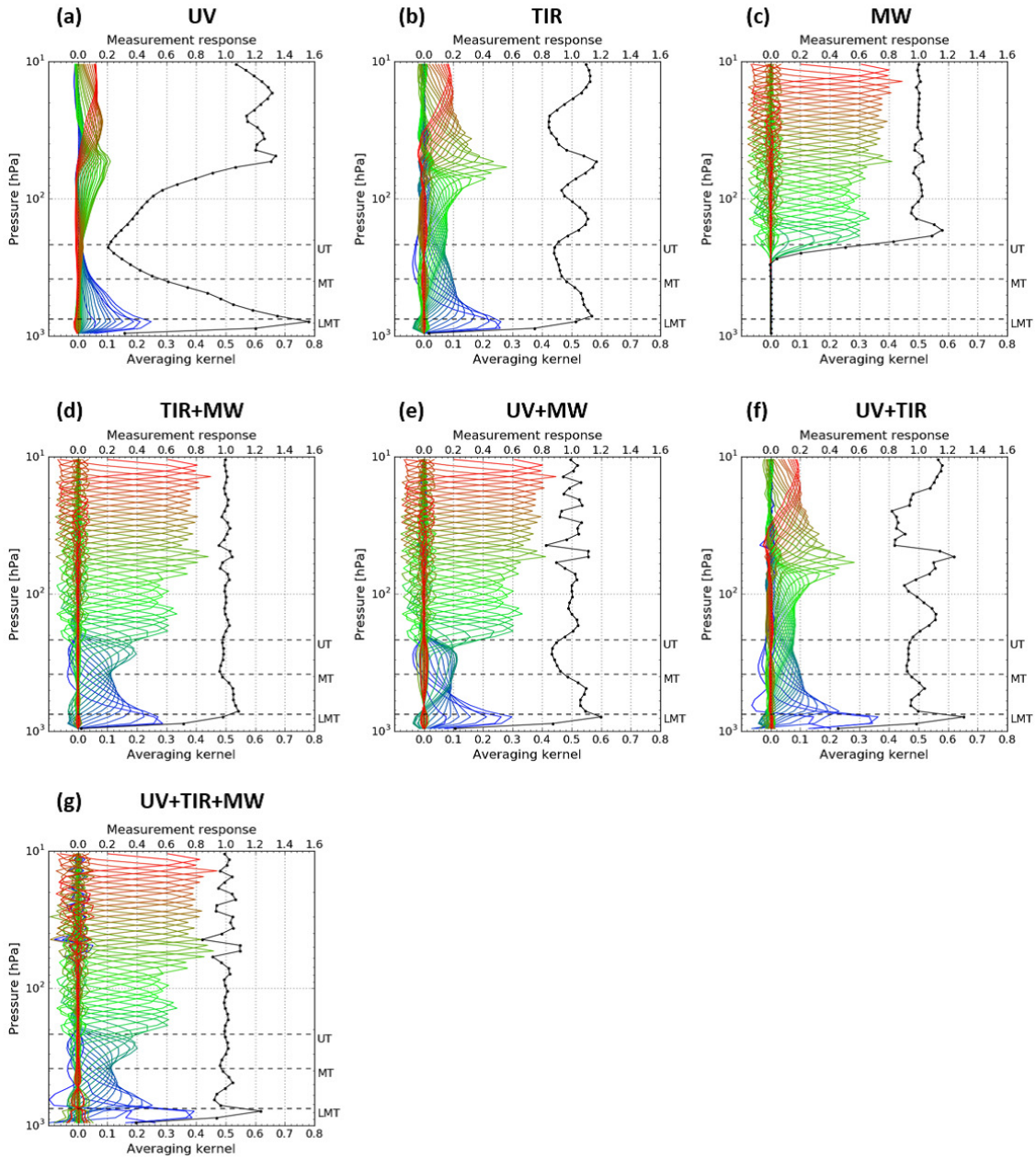


Figure 4. Averaging kernels of the atmospheric profile #01 (June 2009 in CEC) for seven wavelength selection cases: (a) UV, (b) TIR, (c) MW, (d) UV+TIR, (e) UV+MW, (f) TIR+MW, and (g) UV+TIR+MW. The measurement responses are also plotted by black dots and lines. Atmospheric profile #01 is a scenario which has an ozone enhancement in the LMT.

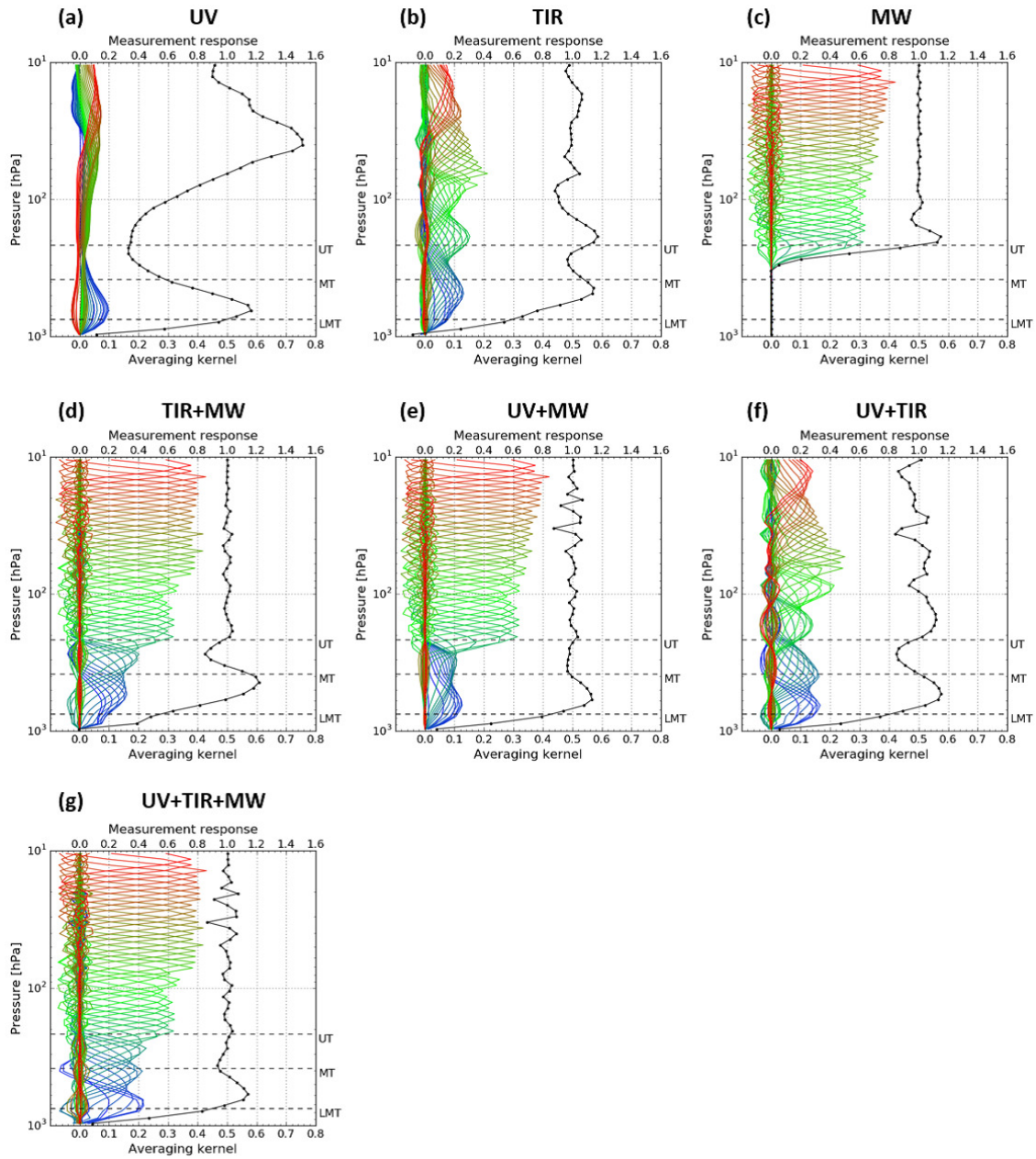


Figure 5. Same as Fig. 4 but for atmospheric profile #12 (December 2009 in CEC). This profile is a scenario that there is less ozone in the LMT.

Table 1. Specifications of the three assumed instruments and the radiative transfer models used in this study.

	UV	TIR	MW
Observation geometry	Nadir-viewing	Nadir-viewing	Limb-viewing
Wavelength	305–340 nm	980–1080 cm^{-1}	345–357 GHz, 639–651 GHz
Spectral resolution	0.6 nm	$\sim 0.12 \text{ cm}^{-1}$	25 MHz
Sampling step	0.2 nm	$\sim 0.12 \text{ cm}^{-1}$	25 MHz
Sensitivity ^a	~ 90 (300 nm), ~ 2600 (340 nm)	300	0.7 K (350 GHz band), 1.7 K (645 GHz band)
Scattering	Yes	No	No
Emission	No	Yes	Yes
Forward model	SCIATRAN	LBLRTM	AMATERASU

^a Instrumental sensitivity is described in the commonly used way for each spectral region; that is, SNR for UV and TIR and noise equivalent brightness temperature for MW.

^b In the case that surface albedo is set to 90 % and solar zenith angle is set to 0° .

Table 2. Summary of 20 atmospheric scenarios used in the simulation.

#	Date ^a	Area ^b	T_s^c [K]	P_s^c [hPa]	PC (UT) ^d [m^{-2}]	PC (MT) ^d [m^{-2}]	PC (LMT) ^d [m^{-2}]	H ₂ O ^e [g/cm ²]
01	6/16	CEC	301.4	976.0	2.57×10^{21}	5.87×10^{21}	5.66×10^{21}	3.4
02	6/24	CEC	304.5	970.2	4.13×10^{21}	6.14×10^{21}	4.51×10^{21}	2.1
03	6/25	CEC	305.0	970.2	3.65×10^{21}	6.52×10^{21}	4.93×10^{21}	2.3
04	6/3	ECS	293.9	999.6	1.49×10^{21}	4.39×10^{21}	3.72×10^{21}	4.5
05	6/9	ECS	294.9	1010.9	1.68×10^{21}	4.17×10^{21}	3.96×10^{21}	4.2
06	6/20	ECS	296.0	1004.2	2.92×10^{21}	6.34×10^{21}	1.86×10^{21}	3.7
07	6/21	ECS	296.5	1002.9	3.00×10^{21}	4.26×10^{21}	2.39×10^{21}	6.0
08	6/26	ECS	296.8	1010.0	3.27×10^{21}	6.20×10^{21}	2.25×10^{21}	4.1
09	6/27	ECS	297.6	1006.6	2.13×10^{21}	3.13×10^{21}	1.49×10^{21}	6.0
10	6/30	ECS	298.1	1004.5	2.71×10^{21}	3.05×10^{21}	1.80×10^{21}	5.9
11	12/2	CEC	280.7	993.1	3.20×10^{21}	4.47×10^{21}	1.83×10^{21}	1.1
12	12/11	CEC	280.0	988.8	2.66×10^{21}	4.38×10^{21}	2.10×10^{21}	1.4
13	12/20	CEC	271.6	997.3	4.58×10^{21}	4.14×10^{21}	2.22×10^{21}	0.3
14	12/22	CEC	278.1	985.9	4.25×10^{21}	4.27×10^{21}	2.21×10^{21}	0.6
15	12/27	CEC	271.3	992.6	4.51×10^{21}	4.41×10^{21}	2.10×10^{21}	0.4
16	12/28	CEC	274.0	985.8	4.12×10^{21}	4.33×10^{21}	2.15×10^{21}	0.4
17	12/4	ECS	286.7	1019.2	4.04×10^{21}	4.48×10^{21}	2.5×10^{21}	1.1
18	12/12	ECS	287.9	1019.9	2.35×10^{21}	4.81×10^{21}	2.92×10^{21}	2.0
19	12/21	ECS	282.4	1025.7	4.91×10^{21}	4.74×10^{21}	2.68×10^{21}	0.8
20	12/26	ECS	281.3	1019.3	3.72×10^{21}	4.38×10^{21}	2.68×10^{21}	0.9

^a All simulation data are from 2009.^b CEC and ECS stand for Central East China (30°N–40°N, 110°E–123°E) and the East China Sea (29°N–33°N, 125°E–129.5°E), respectively.^c Temperature and pressure at the surface.^d PC means ozone partial column. PC is presented for each altitude region: upper troposphere (UT, 215–383 hPa), middle troposphere (MT, 383–749 hPa), and lowermost troposphere (LMT, > 749 hPa).^e H₂O column amount in the troposphere.